Predicting the elastic response of organic-rich shale using nanoscale measurements and homogenisation methods

M. Goodarzi[1], M. Rouainia[1], A.C. Aplin[2], P. Cubillas[2] and M. de Block[3]
[1]*School of Civil Engineering and Geosciences, Newcastle University, Newcastle NE1 7RU, UK.*
[2]*Department of Earth Sciences, Durham University, DH1 3LE, UK.*
[3]*SGS Horizon B.V., Stationsplein 6, Voorburg, 2275 AZ, Netherlands.*

Abstract

Determination of the mechanical response of shales through experimental procedures is a practical challenge due to their heterogeneity and the practical difficulties of retrieving good quality core samples. Here, we investigate the possibility of using multi-scale homogenisation techniques to predict the macroscopic mechanical response of shales, based on quantitative mineralogical descriptions. We use the novel PeakForce Quantitative Nanomechanical Mapping (QNM®) technique to generate high resolution mechanical images of shales, allowing the response of porous clay, organic matter and mineral inclusions to be measured at the nanoscale. These observations support some of the assumptions previously made in the use of homogenisation methods to estimate the elastic properties of shale, and also earlier estimates of the mechanical properties of organic matter. We evaluate the applicability of homogenisation techniques against measured elastic responses of organic-rich shales, partly from published data and also from new indentation tests carried out in this work. Comparison of experimental values of the elastic constants of shale samples with those predicted by homogenisation methods showed that almost all predictions were within the standard deviation of experimental data. This suggests that the homogenisation approach is a useful way of estimating the elastic and mechanical properties of shales, in situations where conventional rock mechanics test data cannot be measured.
Key words: Anisotropy, Elastics, Imaging, Modelling, Rock physics.

1 Introduction

Shale, or mudstone, is the most common sedimentary rock, a heterogeneous, multi-mineralic natural composite consisting of clay mineral aggregates, organic matter and variable quantities of minerals such as quartz, calcite and feldspar. Shale plays a key role as a top seal to many petroleum reservoirs and CO_2 storage sites, as a low permeability barrier for nuclear waste and as an unconventional petroleum reservoir. In all these contexts, and as a material which needs to be effectively drilled when exploring for petroleum, the mechanical properties of shale are critical but quite poorly constrained. For example, there are relatively few laboratory-based studies where mechanical data have been measured on shales which have been well-characterised in terms of mineralogy and microstructure. In part, this is due to the chemical and mechanical instability of shales, which means that it is challenging and expensive to retrieve good quality core samples for undertaking conventional rock mechanics experiments (Kumar, Sondergeld and Rai 2012). Furthermore, because shales are heterogeneous on many scales (e.g. Aplin and Macquaker 2011), it is not straightforward to relate macroscopic experimental measurements to microscopic structural data.

Recently, micromechanical indentation tests have been performed on shales (Zeszotarski et al. 2004; Ulm and Abousleiman 2006). Although this technique is fast and can be performed on commonly available drill cuttings, the data have limited scope as they cannot fully characterize the mechanical response of the material. However, indentation is useful for comparing the mechanical response of different materials. Another approach is to adopt micro-mechanical models that have been widely used in the field of composite engineering (Klusemann, Bohm and Svendsen 2012; Mortazavi et al. 2013). In these methods, the macroscale mechanical behaviour of a composite is determined from the mechanical response of each constituent along with their interaction with each other. This modelling approach is in principle well suited to shale, the mechanical properties of which are likely to depend on the porosity, the volume fraction of solid mineral inclusions and the amount of organic matter (Sayers 2013a).

In their pioneering work on the micro-mechanical modelling of the anisotropic elastic response of shales, Hornby, Schwartz and Hudson (1994) assumed an isotropic intrinsic response for the solid unit of clay into which macroscopic anisotropy was introduced through platelet-shaped clay particles, their orientation and interparticle nanopores. Silt inclusions were then added as spherical isolated grains. Subsequent work modified this approach to provide an improved description of the elastic response of shales, including the incorporation of organic matter into the shale microstructure model (Sayers 1994; Jakobson, Hudson and Johansen 2003; Ortega, Ulm and Abousleiman 2007; Zhu et al. 2012; Vasin et al. 2013; Sayers 2013a; Qin, Han and Zhao 2014). The main difference between these studies relates to the homogenisation strategies used to upscale the shale matrix (containing solid clay, kerogen and fluid phases), as well as the properties of the solid clay and kerogen. For example, Zhu et al. (2012) and Qin et al. (2014) considered kerogen as elliptical inclusions embedded into the shale microstructure. Guo, Li and Liu (2014) followed the same approach as Hornby et al. (1994), combining clay particles with kerogen and adding pores as spherical, isolated inclusions. In contrast, Vernik and Landis (1996) considered kerogen as an isotropic background matrix for the shale, which causes a reduction of the elastic constants. However, Sayers (2013b) showed that a model in which the matrix is described as a transversely isotropic (TI) kerogen and the shale as inclusion provides a better prediction of the elastic stiffness.

Clearly, several quite different modelling approaches have been proposed to explain experimental observations, further highlighting the complexity of shales. In some studies (e.g. Wu et al. 2012; Zu et al. 2013), multiple micro-structural features, such as the amount of pores and their aspect ratios in both clay and kerogen, kerogen particle aspect ratio, cracks, etc., were considered numerically. However, these features could not be directly measured and need to be calibrated. Although it is computationally possible to add any level of detail to a model, it should be noted that different combinations of these micro-structural features can produce the same overall mechanical response. Consequently, it is still difficult to be sure of the micro-structural factors which contribute most to the overall anisotropic response of shales (Bayuk, Ammerman and Chesnokov 2008).

Two key issues need to be resolved in order to successfully implement multi-scale modelling approaches. Firstly, the mechanical properties of the elementary building blocks of shales must be known. Whilst the mechanical properties of phases such as calcite and quartz are reasonably well constrained, those of the solid unit of the porous clay and of organic matter are less well known. The second issue is the selection of an appropriate homogenisation strategy with which to account for the shale micro-structure and capture its behaviour at a macroscopic scale. With these two issues in mind, the objective of the present study is to assess the capabilities of multi-scale homogenisation methods to predict the elastic mechanical response of organic-rich shales using experimental measurements from nano to macro scales. In the first section, the adopted homogenisation formulation is discussed, along with its capabilities and limitations. Having described the input data required for this approach, we then use the recently developed Atomic Force Microscopy (AFM) technique, PeakForce QNM®, to investigate the nanoscale mechanical response

of the individual phases, since these are fundamental inputs to the homogenisation schemes. Published mechanical measurements using Ultra-sonic Pulse Velocity (UPV) test on core samples are then used to evaluate the predictions of the homogenisation method. Finally, indentation moduli measured parallel and perpendicular to bedding in several characterised organic-rich shale samples are used to further test the multi-scale homogenisation formulation for predicting the shale elastic response.

2 Multi-scale homogenisation formulation

Here, shale is assumed to be a composite formed by a porous matrix in which solid mineral grains/inclusions are randomly distributed (Figure 1). As a result, two levels of homogenisation need to be implemented for shales. At the first level, the properties of the shale matrix are upscaled using the porosity and properties of the solid unit of clay and organic matter. At the second level, the macroscale shale behaviour is obtained using the homogenised properties of the porous matrix from the previous level, plus the volume fractions and the properties of the different silt inclusions.

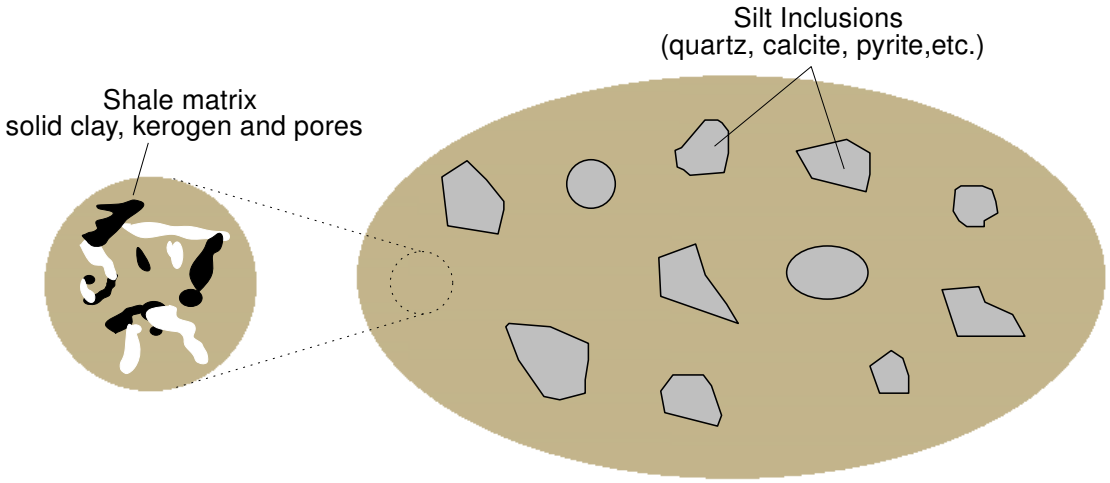

Figure 1: Two levels of shale micro-structure: shale matrix and the matrix-inclusion morphology.

Goodarzi, Rouainia and Aplin (2016) studied the performance and accuracy of various formulations using numerical analyses. Different microstructures for the porous clay and also the matrix-inclusion morphology were considered. Based on these microstructures, numerical models were generated and the macroscale elastic responses were obtained using boundary conditions which replicate uniaxial and hydrostatic compression tests. They conducted numerical simulations of a porous composite in which the shale microstructure ranged from a simple system of one inclusion/void embedded in a matrix, to complex, random microstructures developed from SEM images. They concluded that although the pores are considered as spherical isolated voids in the Self-Consistent Scheme (SCS) (Hill 1965) calculation, the predicted results are in good agreement with porous media with connected or random pore networks. The SCS model also makes a linear prediction for stiffness versus porosity up to a porosity of 0.5, in good agreement with nanoindentation results on porous clay (Ulm and Abousleiman 2006; Bobko and Ulm 2008). Further, Goodarzi et al. (2016) also found that for matrix-inclusion morphologies containing up to 40% of inclusion, the homogenised Young's modulus is better predicted using SCS, whilst the Mori-Tanaka model (MT) (Mori and Tanaka 1973) provides better results for the homogenised bulk modulus. For volume fractions above 40%, the prediction error for these schemes increases gradually. Overall, these results suggest that SCS can be adopted for the first level of homogenisation.

Several formulations have been proposed to upscale the elastic response of a composite, each making certain assumptions about the geometry of, and interaction between the various constituents. A key challenge is to select a formulation which best captures the macroscopic behaviour.

The closed-form solution for the SCS is obtained by assuming that a single inclusion is embedded in a homogenised composite. Within this formulation, no single phase is considered to act as the matrix and all the phases are given equal importance. The derived nonlinear equation requires an iterative procedure to be solved for the homogenised elastic stiffness tensor and is given as follows:

$$\mathbb{C}_{\text{hom}} = \sum_{r=1}^{N} f_r \mathbb{C}_r : \left[\mathbb{I} + \mathbb{P}_{\text{I}_\text{r}}^{\text{hom}} : (\mathbb{C}_r - \mathbb{C}_{\text{hom}})\right]^{-1} \tag{1}$$

where $\mathbb{C}_{\text{hom}}$ is the fourth order stiffness tensor for the composite, $\mathbb{C}_r$ is the stiffness tensor and f_r is the volume fraction of the phase r, N is the total number of phases, $\mathbb{I}$ is the symmetric identity tensor, and $\mathbb{P}_{\text{I}_\text{r}}^{\text{hom}}$ is the Hill tensor which depends on the shape and the properties of the phase and the homogenised stiffness tensor of the composite. The stiffness tensor for a transversely isotropic material is described in terms of five independent components which can be written in the matrix notation as:

$$\mathbb{C} = \begin{bmatrix} C_{11} & C_{12} & C_{13} & 0 & 0 & 0 \\ C_{12} & C_{11} & C_{13} & 0 & 0 & 0 \\ C_{13} & C_{13} & C_{33} & 0 & 0 & 0 \\ 0 & 0 & 0 & 2C_{44} & 0 & 0 \\ 0 & 0 & 0 & 0 & 2C_{44} & 0 \\ 0 & 0 & 0 & 0 & 0 & 2C_{66} \end{bmatrix} \quad \text{with} \quad C_{66} = \frac{1}{2}\big(C_{11} - C_{12}\big) \tag{2}$$

The MT scheme, on the other hand, is based on the assumption that the inclusion is embedded in a layer of the matrix and an additional interaction term takes into account the effect of the adjacent inclusions. The final expression for MT scheme can be written as:

$$\mathbb{C}_{\text{hom}} = \sum_{r=1}^{N} f_r \mathbb{C}_r : \left[\mathbb{I} + \mathbb{P}_{\text{I}_\text{r}}^{0} : (\mathbb{C}_r - \mathbb{C}_0)\right]^{-1} \left[\sum_{s=0}^{N} f_s \left[\mathbb{I} + \mathbb{P}_{\text{I}_\text{s}}^{0} : (\mathbb{C}_s - \mathbb{C}_0)\right]^{-1}\right]^{-1} \tag{3}$$

where $\mathbb{C}_0$ is the stiffness tensor for the matrix phase, and $\mathbb{P}_{\text{I}_\text{s}}^{0}$ is the Hill tensor which here it depends on the shape and the properties of the phase r and the homogenised stiffness tensor of the matrix. Obtaining the Hill's tensor for the case of an anisotropic matrix is not trivial as it requires determination of Green's function, which is extremely complicated for transversely isotropic materials (Laws 1977). Laws (1977) derived an integral expression for Hill's tensor in this particular case which does not require knowledge of Green's function. For explicit formulae of Hill's tensor components for a spherical inclusion embedded in transversely isotropic matrices, readers are referred to Fritsch and Hellmich (2007). To the best of our knowledge, this is the only reference providing these expressions correctly.

3 Material properties

From equations (1) and (3), it can be seen that the volume fractions and the stiffness tensors of all constituents are required to allow the calculation of the homogenised elastic response of the composite. The volume fraction and mineralogy of clay and mineral inclusions can be estimated using X-ray diffraction, and the amount of organic matter measured by chemical analysis. A good estimation of the porosity, which can be measured in various ways, is also essential to the calculation of the clay matrix properties. The entire porosity of the sample is assumed to exist in the shale matrix, so that the porosity of the this matrix, ϕ_{matrix}, which is used in the first level of homogenisation, is calculated as:

$$\phi_{matrix} = \frac{\phi_{shale}}{1 - f_{inc}} \tag{4}$$

where ϕ_{shale} represents the shale porosity and f_{inc} is the total volume of non-clay minerals. For dry conditions, porosity is taken to be a constituent with zero stiffness. However, in fully saturated shale, the stiffness properties of water within pores (i.e. bulk stiffness $K = 2.2$ GPa and shear stiffness $G = 0$ GPa) needs to be considered (Hornby et al. 1994; Vasin et al. 2013).

Model implementation requires certain assumptions to be made about the properties of the different phases in shale. The shape and orientation of both inclusions and pores are generally considered to be important sources of the macroscopic anisotropic response of shales (Vasin et al. 2013). Nanoscale indentation tests performed on several shale samples with a different level of porosity in their clay matrices revealed that the solid part of the porous clay exhibits a significant, intrinsic, anisotropic elastic response which gradually reduces with increasing porosity (Ulm and Abousleiman 2006; Bobko and Ulm 2008). O Ortega, Ulm and Abousleiman (2010) used a micro-mechanical approach to study the simultaneous effects of (a) anisotropy of the porous clay matrix, which was assumed to originate from solid clay particles, and (b) the shape and orientation of silt inclusions on the transversely isotropic elastic

behaviour of bulk shale. They concluded that the possible contribution of the shape and orientation of silt inclusions on the macroscopic anisotropy of the shale is insignificant compared to the anisotropy of the clay matrix. This theoretical approach is also consistent with previous modelling and experimental studies in which an inverse correlation between silt inclusion content and anisotropy has been demonstrated (e.g. Bayuk et al. 2008; Guo et al. 2014).

In addition, incorporating the effect of inclusion shape into multi-scale homogenisation requires additional experimental data which makes this approach inefficient from a practical point of view.

Here, inclusions such as quartz, calcite, pyrite, etc, are considered to be spherical and to have isotropic elastic moduli which can be found in the literature (Table 1). The solid unit of porous clay, on the other hand, is assumed to be anisotropic; furthermore, its properties cannot be directly measured using conventional rock mechanics tests. Ortega et al. (2007) assumed that the overall anisotropy of shale originates from a solid unit of clay with universal mechanical properties. The elastic constants of the solid unit of clay as a transversely isotropic material were estimated by back-analysing from UPV measurements on shale core samples. It should be noted that this solid phase could be an agglomerate of clay particles. Table 2 provides the values obtained by Ortega et al. (2007).

Table 1: Properties of common minerals in shales (Bass 1995; Mavko, Mukerji and Dvorkin 2009; Whitaker et al. 2010).

Minerals	Elastic properties	
	E (GPa)	Poisson's ratio
Quartz	101	0.06
Calcite	95	0.28
Pyrite	265.4	0.18
Feldspar	73.7	0.26
Dolomite	118	0.29

The assumption that only one set of elastic constants can be used for the solid unit of clay (e.g. Ortega et al. 2007; Table 2), regardless of mineralogy, is debatable and so it is of interest to compare Ortega et al.'s values with those used in previous studies. Hornby et al. (1994) back-calculated the solid clays elastic constants from an experimental data set on clay-fluid composite as $K = 22.9$ GPa and $G = 10.6$ GPa, assuming isotropic conditions. Similar values of $K = 25$ GPa and $G = 9$ GPa are provided in Mavko et al. (2009). These values have been adopted in several micromechanical models of shales with satisfactory results, regardless of the clay mineralogy (Jakobsen et al. 2003; Draege, Jakobsen and Johansen 2006; Wu et al. 2012; Sayers 2013a; Qin et al. 2014; Guo et al. 2014). Converting the anisotropic properties in Table 2 using the Voigt average (Antonangeli et al. 2005) to its equivalent isotropic form results in comparable values of $K = 23.9$ GPa and $G = 6.7$ GPa. Considering these micromechanical models and also nanoindentation test data (Ulm and Abousleiman 2006), the assumption of constant properties for the elementary building block of porous clay can be adopted confidently. Additionally, it should be noted that the presented values are still much lower than the ones obtained for a single clay particle (Wang, Wang and Cates 2001). Bobko and Ulm (2008) justified this difference by assuming that the porous clay has a nano-granular microstructure. They concluded that the mechanical response of porous clay might be mainly determined by chemical and mechanical interactions in contacts between individual clay particles or clay agglomerates, rather than the intrinsic mechanical response of a single clay particle.

Table 2: Solid clay properties (data from Ortega et al. 2007).

Elastic Constant	Value (GPa)
C_{11}	44.9
C_{33}	24.2
$\mathbf{C}_{13}$	18.1
C_{66}	11.6
C_{44}	3.7
C_{12}=$\left(C_{11} - 2C_{66}\right)$	21.7

Shale gas and oil reservoirs contain significant amounts of organic matter, which has a wide range of measured elastic properties. Zeszotarski et al. (2004) performed nanoindentation tests on kerogen in Woodford shale. An

isotropic behaviour was observed and if Poisson's ratio is assumed to be 0.3, then the Young's modulus is estimated to be 11.5 GPa. The same approach was adopted by Kumar (2012) and Zargari et al. (2013), who generated values of less than 2 GPa for highly porous kerogen. Vernik and Nur (1992) used the thin-layer composite concept and back-analysed the mechanical properties of kerogen, concluding that kerogen is isotropic with values of 8 GPa and 0.28 for the Young's modulus and the Poisson's ratio, respectively. Yan and Han (2013) used effective medium theory and back-calculated the Young's modulus of 4.5, 6.42, 10.7 GPa for immature, mature and overmature organic matter, respectively. Eliyahu et al. (2015) performed PeakForce QNM® tests with an atomic force microscope to make nanoscale measurements of the Young's modulus of organic matter in a shale thin section. Results ranged from 0-25 GPa with a modal value of 15 GPa. Due to the relative softness of organic matter, the mechanical behaviour of shales may be significantly influenced by even small amounts of organic matter (Vernik and Milovac 2011; Sayers 2013b). This can lead to difficulties in implementing homogenisation techniques for these materials.

4 Nanoscale mechanical mapping of shales

Since shales are mainly formed of particles which range in size from smaller than 0.1 microns to 100 microns, it follows that a high resolution technique is required to measure the mechanical properties of individual particles or constituents in situ. Conventional small-scale mechanical testing methods such as indentation can extract discontinuous data, but only at a resolution of at least several microns. In contrast, the recently developed AFM technique known as PeakForce QNM® is a non-destructive method which measures the elastic response of a material surface with a resolution of a few nanometres. In this mode, an AFM probe is tapped over the surface (using a sinusoidal signal) and the peak force applied on the surface is used as a feedback parameter to track the scanned surface (i.e. the peak force is continuously monitored and kept constant during scanning). The mechanical response of the sample is extracted using the generated force-separation curve (one for every approach-withdraw cycle). The reduced Young's modulus can be calculated by fitting the Derjaguin-Muller-Toporov (DMT) model for contact mechanics on the curve obtained through the retracting stage of the tip movement (see Figure 2). According to this model the relationship between peak force (F_{pf}), adhesion force (F_{adh}) and the reduced Young's modulus, E^*, is as follows:

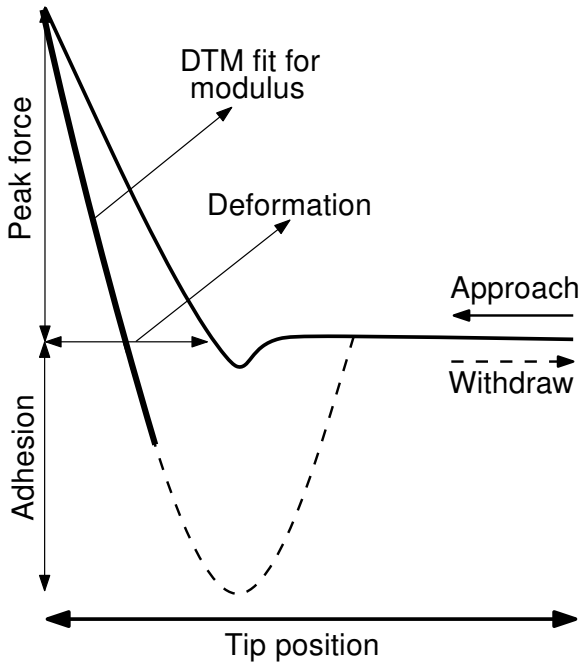

Figure 2: Schematic diagram of a generated force-separation curve for a single tapping of the PeakForce QNM® (Modified from Bruker's Application Note #128).

$$F_{pf} - F_{adh} = \frac{4}{3} E^* \sqrt{R(d - d_0)^3} \tag{5}$$

where R is the tip radius and $(d - d_0)$ is the sample deformation. The modulus obtained from equation (5) can be related to the sample elastic response as:

$$E^* = \left(\frac{1 - \nu_s^2}{E_s} + \frac{1 - \nu_{tip}^2}{E_{tip}} \right)^{-1} \tag{6}$$

where E is the Young's modulus, ν is the Poisson's ratio and subscripts s and tip represent the sample and tip, respectively.

In order to achieve reliable data several calibration procedures should be performed. First, the effective tip radius is determined by probing a polycrystalline titanium standard sample. Second, the deflection sensitivity of the cantilever is measured by pushing the tip against a sapphire sample which serves as a surface with approximately infinite stiffness. The spring constant of the tip is also required, and in this case was provided by the manufacturer (Bruker). Finally, the calibrated system is evaluated against a standard pyrolitic graphite sample (HOPG-12, Bruker) with a known mechanical response. For more information about the background theory and calibration procedure of PeakForce QNM® readers are referred to Trtik, Kaufmann and Volz (2012), Bruker's Application Note #141 and Bruker's Application Note #128.

After performing all the essential adjustments and calibration, PeakForce QNM® was implemented to generate a high-resolution mechanical image of shale. For this purpose, an organic-rich shale sample was characterised and two sections, parallel and perpendicular to the bedding plane, were prepared (Table 3). Since a smooth surface is a key condition for good quality data in PeakForce QNM® and Indentation tests, the surfaces were hand polished and then polished using argon ion milling (Amirmajdi et al. 2009). Additionally, a suitable cantilever-tip assembly (with a relatively large stiffness > 200 Nm^{-1}) is required to be able to measure the modulus on a shale, which contains stiff mineral grains ($E > 50$ GPa) such as quartz. A diamond tip with a spring constant of 272 Nm^{-1} (DNISP; Bruker) was selected for this study. The tip was oscillated with 1 kHz frequency and the peak force was set to $50 - 150$ nN, as this provided the best results during the tests performed on the HOPG-12 standard. These settings generated 1-2 nm indentation depths on the sample.

Table 3: Characterisation of shale sample for the PeakForce QNM® test.

Mineralogy	Volume fraction (%)
Quartz	16.78
Calcite	0.23
Pyrite	2.91
Feldspar	0.59
Dolomite	0.00
Clay	65.97
Total organic carbon (TOC)	Weight (%) 5.83
Porosity	9.45

4.1 Nano-mechanical image analysis

Figure 3 shows the elastic modulus map obtained on a 25×25 μm^2 area on the shale sample perpendicular to the bedding direction (Figure 3d). Two types of grains with different, and relatively high stiffness (> 50 GPa); and also areas with very low stiffness (< 30 GPa) can be clearly recognised in this image. In order to better interpret the elastic modulus map, more analyses including back-scattered electron (BSE) SEM imaging, energy dispersive spectroscopy (EDS) chemical analysis and topographical data were also obtained from the same area (Figure 3). As part of the data analysis, it was initially assumed that the stiffer grains represent pyrite (and were later identified as such from the EDS analysis (Figure 3b). An average value above 100 GPa was measured on pyrite grains which is lower than the reported values of 265 GPa in the literature (see Table 1). The main reason for this deviation is that the reliable range of measurable elastic modulus for the diamond tip is less than 80 GPa (Bruker's Application Note #128). The mean value of the measured Young's modulus over the grains corresponding to quartz in the EDS analysis (Figure 3b) is around 75 GPa, lower than the value reported in Table 1 but between the values reported by Elihayu et al. (2015), 63 ± 8 GPa, and Mavko et al. (2009), $77 - 95$ GPa. Again, it is difficult to be certain of this result because of the reliable range of the tip.

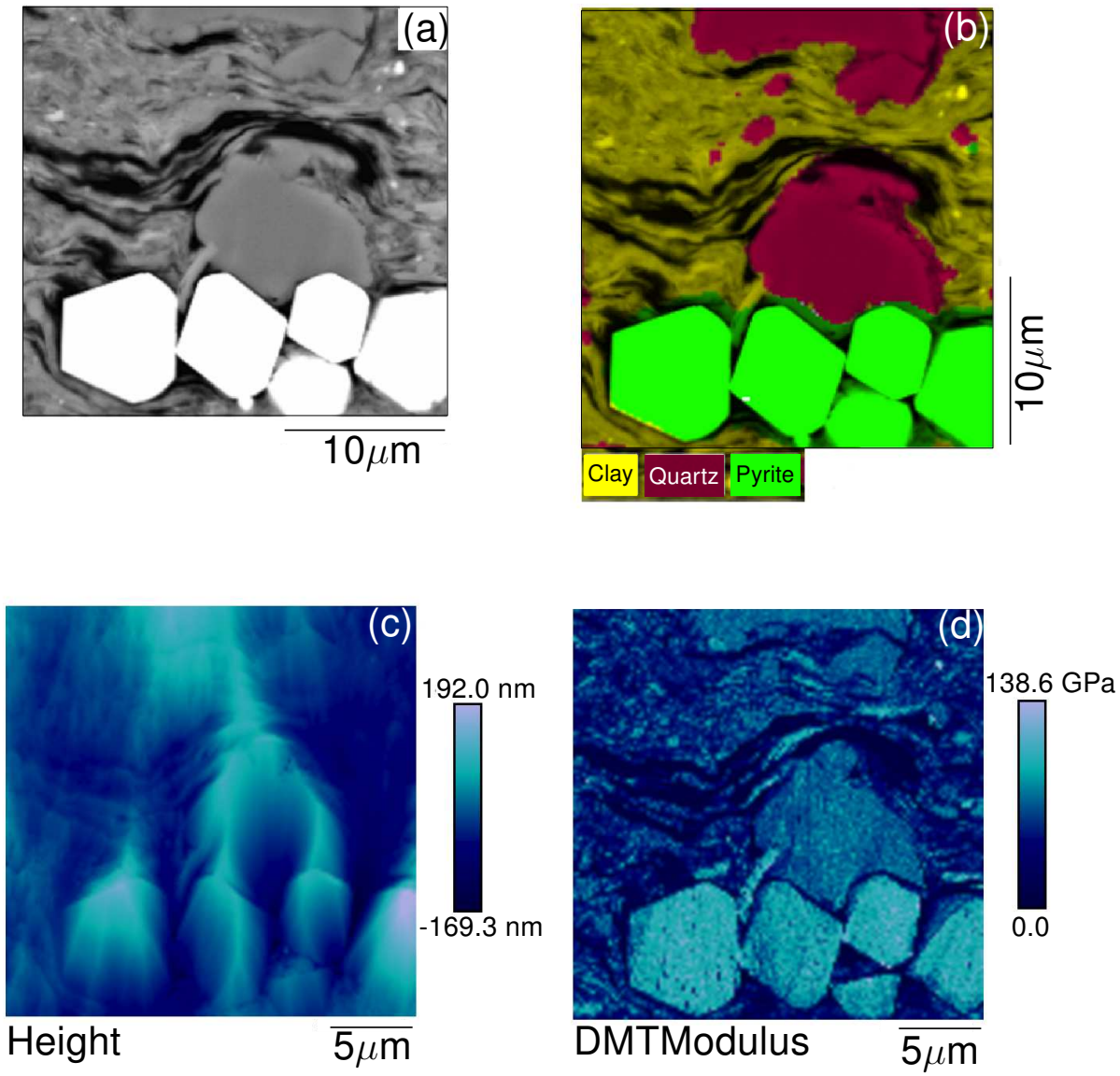

Figure 3: Different analyses on a target area perpendicular to the bedding direction. (a) SEM image using back scattered electron (BSE) imaging, (b) chemical analyses using energy dispersive spectrometry (EDS), (c) topography map taken during mechanical mapping and (d) Young's modulus map using PeakForce QNM®.

Due to the stiffness difference of shale constituents, it is not possible to prepare a surface as smooth as single phase materials such as the pyrolitic graphite sample which is used for the calibration. Sample roughness may yield unreliable data. Comparing the topographical and the mechanical maps (Figures 3c and 3d), it can be concluded that some soft areas are correlated with abrupt deep areas on the sample. In fact, unlike the interpretation made by Eliyahu et al. (2015), not all the soft regions can be attributed to organic matter and a careful comparison between both the mechanical and topographical images is required to locate real soft phases in the mechanical image. Such a comparison revealed the fact that the presence of the organic matter phase in the shale composite is not similar to other inclusions such as quartz and pyrite. This phase is intimately mixed within the porous clay rather than existing as isolated grains; this is important when accounting for organic matter in the homogenisation techniques. Assuming Poisson's ratio is 0.3 for this phase, the measured Young's moduli are less than 10 GPa with a mean value of 6 GPa. Considering that the maturity of this sample is at a vitrinite reflectance of $0.5 - 0.6\%$ (Ro), this result is consistent with the values of $6 - 9$ GPa for immature kerogen obtained by Kumar (2012).

As the macroscopic response of shales is highly anisotropic, it is of interest to look at anisotropy at the nanoscale. Figure 4 shows the Young's modulus map of sections both parallel (E_1) and perpendicular (E_3) to the bedding direction. Two target areas were selected on both images that contained porous clay and quartz grains. The measured data in these areas were extracted and subjected to statistical analysis. Figure 5 illustrates the histogram and normal curve on the data and the mean values and standard deviations (SD) are provided in Table 4.

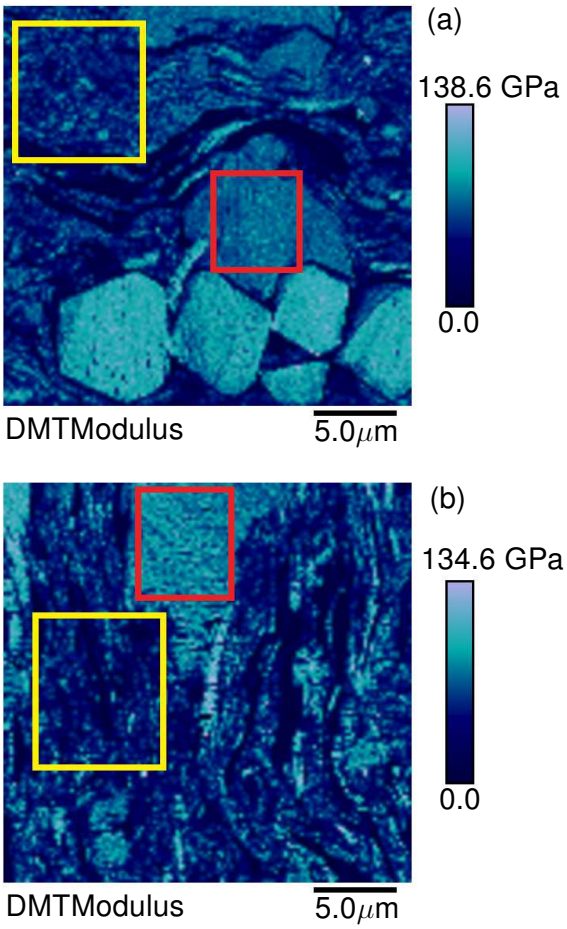

Figure 4: Yellow boxes are the target areas for porous clay and red boxes are the target areas for quartz on sections perpendicular (a) and parallel (b) to the bedding direction.

The mean values obtained on quartz grains are almost identical, producing an anisotropy ratio (E_1/E_3) around 0.95. Although the measurements were taken from two different grains with unknown orientations, this can be interpreted as an isotropic response for this phase. The observed, in situ elastic response of quartz grains within shale microstructure is different to measurements on large quartz crystals, which show noticeable anisotropy (Heyliger, Ledbetter and Kim 2003). Vasin et al. (2013) considered the full anisotropic elastic response of silt inclusions with random orientations in modelling shale anisotropy. However, since quartz grains in shales are randomly orientated with respect to the crystal structure, our observation supports the simple assumption made in Hornby et al. (1994)

that accounts for mineral inclusions as a spherical, elastically isotropic phase.

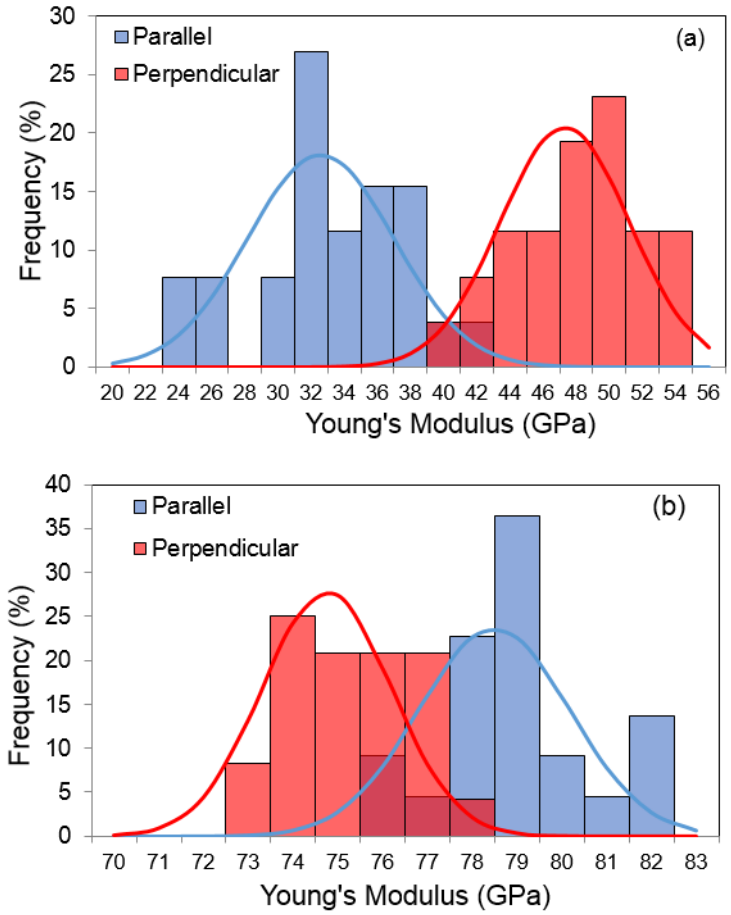

Figure 5: Histogram and normal curve of the measured Young's moduli on (a) porous clay and (b) quartz grain in both sections parallel and perpendicular to bedding direction.

The porous clay, on the other hand, shows significant anisotropy in these two sections with a ratio (E_1/E_3) around 1.45. An anisotropic ratio of 1.54 was obtained for a shale sample with almost the same porosity and inclusion volume fraction using UPV measurement on core samples (Ulm and Abousleiman 2006). This comparison provides more support for the assumption, discussed in Section 3, about the origin of shale anisotropy. Additionally, the values obtained on the porous clay are higher than the properties assumed for a solid unit of porous clay here or the properties obtained by Hornby et al. (1994) (Table 2), but they are within the range of the properties reported for clay particles (Wang et al. 2001). Eliahayu et al. (2015) reported 29 $\pm$ 1 GPa on the porous clay while they did not consider the direction of the section in their study. This value is very close to the measured data on the section perpendicular to bedding (see Table 4). Further study is required to understand what type of micro-component of the porous clay was being touched by the tip.

Table 4: Statistical analysis of measured data on target areas containing porous clay and quartz grains.

Parameter	Young's modulus				Anisotropy ratio (E_1/E_3)
	Parallel to bedding (E_1)		Perpendicular to bedding (E_3)		
	Mean (GPa)	SD	Mean (GPa)	SD	
Quartz grains	74.75	1.43	78.5	1.70	0.95
Clay matrix	47.3	3.88	32.5	4.41	1.45

5 Implementation of multi-scale homogenisation techniques

The capabilities of homogenisation techniques in shales was investigated using numerical simulations in which several virtual shale microstructures were generated and studied (Goodarzi et al. 2016). Good agreement was obtained between macroscopic elastic responses of the numerical rocks and the predicted values from the homogenisation methods.

However, it is clear that real composites, especially shales, are far more complex than the assumed numerical models and consequently it is important to validate the homogenisation techniques against several experimental data sets. Whilst UPV tests have been used to fully characterize the elastic response of shale samples, the experiment requires good quality core samples and is both technically difficult and time-consuming. Recently, indentation tests have been used to estimate the mechanical properties of shales. This test can be easily and efficiently performed on shale cuttings and a good estimation on the anisotropic macroscopic elastic response of shale can be obtained (Kumar et al. 2012; Ulm and Abousleiman 2006). Here, published UPV results on well-characterised shales are used to evaluate the predictive capability of the homogenisation techniques. In addition, several organic-rich shale samples were prepared, characterized and used to generate indentation data in order to extend the validation data sets.

5.1 Elastic response of shales porous clay

The mechanical response of silt-grade mineral inclusions in shales are well known and possible shape effects can be quantified using SEM or 3-D X-ray microtomographic imaging (Kanitpanyacharoen et al. 2011; Vasin et al. 2013; Peng et al. 2015). However, neither the exact microstructure of the porous clay, nor the properties of the solid unit of this composite, have been fully evaluated. A complex network of pores including connected channels and isolated pores at different scales have been experimentally observed in porous clay (e.g. Chalmers, Bustin and Power 2012). Similarly, the organic matter occurs as a semi-continuous phase rather than as isolated inclusions in the porous clay (see Figure 3). Consequently, the main challenge in modelling the elastic behaviour of shales is the response of the matrix.

The main assumption in our approach is that the anisotropy originates from the solid clay, having a transversely elastic response. The Self-Consistent Scheme is used to combine, without any specific orientation distribution, the solid clay with the presence of pores and organic matter. Aligned, platy clay minerals are not considered explicitly and the TI response compensates for this effect. On the other hand, Hornby et al. (1994) assumed an isotropic response for the solid clay and the anisotropy was subsequently generated by considering an oblate spheroid-shaped clay particles and nanopores. The SCS was combined with a differential effective medium model in order to satisfy the continuity of all the phases at any porosity level.

In order to clarify similarities and differences between the approach adopted in this paper and the pioneering work of Hornby et al. (1994), all five elastic constants of a fully-saturated porous clay are plotted as a function of porosity in Figure 6. Both approaches provide a similar trend for the elastic constants as functions of fluid-filled porosity except for C_{44}, which shows a drastic decrease with a small increase in porosity in the Hornby et al. (1994) formulation. Additional differences can be partly attributed to the initial assumptions with regard to the isotropy and anisotropy of the elastic properties of the solid unit of clay. It should be noted that an increase or decrease in anisotropy can of course be introduced by considering elliptical shapes with specific orientations for pores or organic matter in the SCS formulation. These two modelling approaches give quite consistent results in reproducing the response of porous clay.

5.2 UPV test data sets

There are very few measurements of the mechanical behaviour of shales which are well characterised in terms of both mineralogy and microstrcture. Among these available data, those which were not used by Ortega et al. (2007) to back-calculate the stiffness of the solid unit of porous clay, were chosen for this study. Table 5 provides the mineralogical descriptions of these samples. For the first two data sets, Kimmeridge and Jurassic shales, the elastic constants were measured in saturated conditions under different confining pressures. With increasing confining pressure, properties almost converged to constant values which we infer are due to the closure of microcracks. As cracks are not considered in our modelling, the values corresponding to the highest confining pressure, 80 MPa, were selected for comparison. For Woodford shales the natural water content of the samples was preserved but no information was provided on the confining pressure.

The transversely isotropic elastic stiffness tensors were obtained for these four shales using UPV tests conducted on core samples. The mineralogical data provided in Table 5 were used along with homogenisation methods to

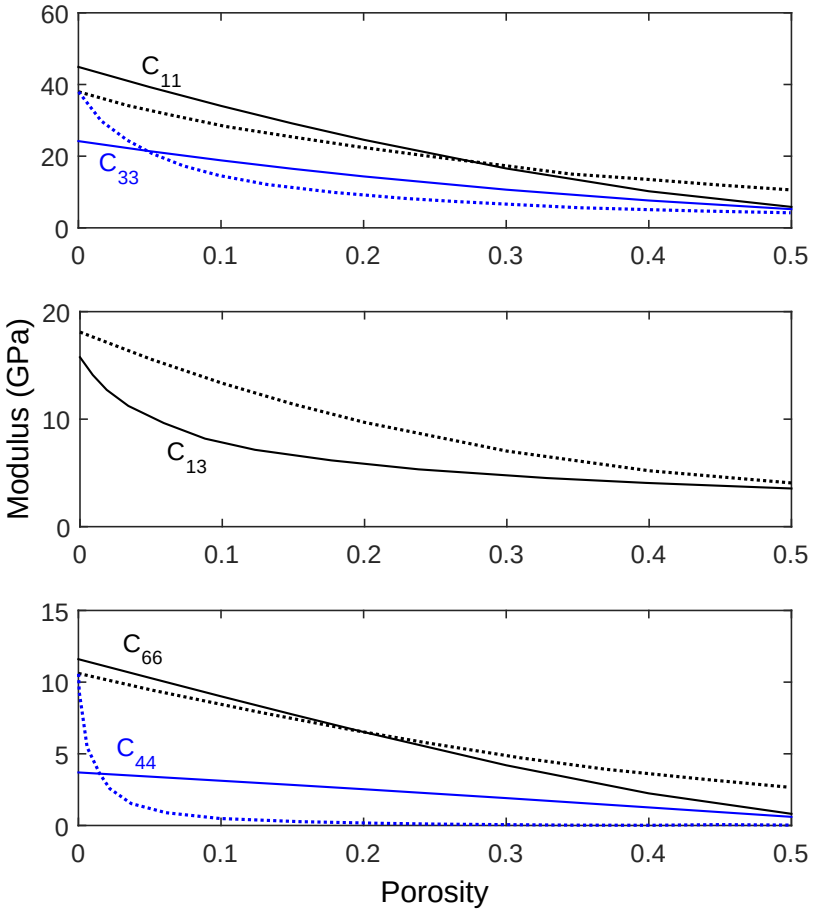

Figure 6: Saturated porous clay response versus porosity (solid lines are the results of this paper and dashed lines were extracted from Hornby et al. 1994).

Table 5: Mineralogical data for the UPV data sets shale samples (extracted from Hornby 1998; Sierra et al. 2010)

Sample	Kimmeridge Shale	Jurassic Shale	Woodford-1 Shale	Woodford-2 Shale
Mineralogical Data	Volume Fraction (%)			
Quartz	30.5	31	-	-
Calcite	-	1	-	-
Pyrite	2.1	5	-	-
Feldspar	7.2	4	-	-
Dolomite	-		-	-
Clay	60.2	58	57.1	65.2
Sum of Non-Clay	39.8	42	42.9	34.8
Shale Porosity	2.5	10.5	16	15
Clay Porosity	4.15	18.1	28	23

estimate the five elastic constants for each sample. The SCS was adopted for the first stage of homogenisation. Both MT and SCS formulations were implemented for the second stage, in which matrix-inclusion morphology is homogenised, in order to evaluate which strategy results in better predictions of macroscale mechanical behaviour. In addition, the elastic properties of quartz were used to homogenise samples for which only the volume fraction of non-clay minerals are available, as this mineral is usually the most common non-clay mineral in shales. Figure 7 illustrates the predicted and the experimental results of the elastic constants of transversely isotropic shales using both SCS-SCS and SCS-MT strategies with bars showing the experimental standard deviation for each constant. The values of these constants, Thomsen's anisotropy parameters of $\varepsilon = (C_{11} - C_{33})/2C_{33}$ and $\gamma = (C_{66} - C_{44})/2C_{44}$ and their relative errors (%) are also given in Tables 6 and 7.

Comparing the relative errors between two up-scaling strategies revealed that there is no clear superiority for one strategy over the other one. This result can be justified due to the fact that each component of the stiffness tensor is a combination of two elastic constants; for example for an isotropic material $C_{11} = E(1-\nu)/((1+\nu)(1-2\nu))$. As it was highlighted in Section 2, numerical studies using SCS and MT schemes for predicting homogenised elastic response of matrix-inclusion morphology showed that each of this elastic constant can be better predicted with one of these schemes (Goodarzi et al. 2016). In fact, the error observed in homogenised stiffness tensor components can be seen as the combined error of homogenised elastic constants. It can be observed that both SCS-SCS and SCS-MT methods produce some theoretical errors. However, in general, it can be concluded that SCS-SCS performed slightly better, particularly in terms of capturing anisotropy.

Table 6: Experimental (Exp) and predicted (Pred) elastic constants for the UPV data sets samples using SCS-SCS.

Elastic constant	Kimmeridge Shale			Jurassic Shale			Woodford-2 Shale			Woodford-2 Shale		
	Exp.	Pred.	Error (%)	Exp.	Pred.	Error (%)	Exp.	Pred.	Error (%)	Exp.	Pred.	Error (%)
C_{11} (GPa)	56.2	56	0.35	46.1	45.3	1.73	25	35	40	28.3	34.6	22.2
C_{33} (GPa)	36.4	37	1.64	32.9	31.7	3.64	18.6	26	39.7	18.6	23.5	26.
C_{13} (GPa)	20.5	17.2	16.1	18.5	13.3	28.1	6.9	9.96	44.3	9.8	10.6	8.16
C_{66} (GPa)	18.9	18.2	3.70	14.3	15	4.9	7.8	11.8	51.2	9.3	11.1	19.3
C_{44} (GPa)	10.3	10.2	0.97	8.8	9.5	7.95	5.7	8.2	43.8	5.5	6.6	20
ε	0.27	0.26	5.5	0.2	0.21	6.9	0.17	0.17	0.0	0.26	0.23	9.4
γ	0.41	0.39	6.0	0.31	0.29	7.3	0.18	0.21	19	0.34	0.34	0.0

Table 7: Experimental (Exp) and predicted (Pred) elastic constants for the UPV data sets samples using SCS-SCS.

Elastic constant	Kimmeridge Shale			Jurassic Shale			Woodford-2 Shale			Woodford-2 Shale		
	Exp.	Pred.	Error (%)	Exp.	Pred.	Error (%)	Exp.	Pred.	Error (%)	Exp.	Pred.	Error (%)
C_{11} (GPa)	56.2	54.2	3.55	46.1	41.6	9.76	25	30.6	22.4	28.3	32.5	14.8
C_{33} (GPa)	36.4	33.5	8	32.9	26.4	19.7	18.6	20.6	10.7	18.6	20.7	11.2
C_{13} (GPa)	20.5	17.6	14.1	18.5	13.3	28.1	6.9	10.1	46.3	9.8	10.8	10.2
C_{66} (GPa)	18.9	17	10	14.3	13	9.1	7.8	9.5	21.7	9.3	9.9	6.45
C_{44} (GPa)	10.3	8.1	21.3	8.8	6.7	23.8	5.7	5.4	5.26	5.5	5.1	7.3
ε	0.27	0.31	0.13	0.2	0.28	43.5	0.17	0.24	41	0.26	0.28	9.3
γ	0.41	0.54	31.5	0.31	0.47	50.4	0.18	0.37	106	0.34	0.47	36.2

The prediction errors are relatively lower for the elastic constants C_{11} and C_{33} compared to those for C_{13}. This can be explained by the high degree of measurement uncertainties in C_{13} where the standard deviations are usually expected to be between 30% and 50% (Jones and Wang 1981; Domnesteanu, McCann and Sothcott 2002; Jakobsen and Johansen 2000). Additionally, Sayers (2013a) studied the anisotropic response of shales and concluded that the value of C_{13} can be affected by features such as the presence of microcracks in the sample, which is ignored in our model. Considering the complexity of shale microstructure in addition to the high standard deviations which are usually observed when measuring shale properties, we conclude that the homogenisation methods can provide valuable mechanical results simply and inexpensively, using just quantitative mineralogical descriptions of shales.

The data in Table 7 show that the anisotropy was captured very well for all the data sets. However, it is obvious that the absolute predicted elastic constants are not satisfactory for the case of Woodford shales in comparison with the results obtained for Kimmeridge and Jurassic shales. As the homogenisation overestimates the elastic modulus, this could be due to the lack of information on the confining pressures used in the Woodford data sets. This is a critical parameter in the UPV test results as it can reduce the effect of microcracks, which are not considered in the modelling. For example, elevation in confining pressure from 5 MPa to 80 MPa increases C_{11} by 40% in Jurassic shale (Hornby 1998). The TOC contents of these samples were not provided in the reference which could also have significantly reduced the elastic response. Moreover, it is also of interest to compare these results with previous micro-mechanical modelling of the same data sets. Jakobsen et al. (2003) attempted to predict the Jurassic shale elastic response. Several strategies were tried and the best results they could achieve were close to the measured properties at a confining pressure of 20 MPa. Vasin et al. (2013) started with a single clay particle to build up a shale model for Kimmeridge shale. They could not manage to reproduce the elastic response using the shale characterization obtained experimentally. By increasing the porosity to more than 10% with a specific aspect ratio, a good agreement was achieved with the predicted results and the measured elastic constant at a confining pressure of 80 MPa. It should be emphasised that the predicted data here are obtained solely using the shale characterisation presented in the literature (Hornby 1998; Sierra et al. 2010), without any further calibration.

5.3 Indentation data sets

5.3.1 Indentation test

Indentation tests generate mechanical properties of materials from their surface response. In this test, an indenter with known mechanical properties is pushed into a material surface with unknown properties. The continuous loading and unloading curves versus displacement are plotted as depicted in Figure 8, and two material properties can be defined as follows:

$$H = \frac{F_{max}}{A_c} \tag{7}$$

$$M = \frac{\sqrt{\pi}}{2}\frac{S}{\sqrt{A_c}} \quad \text{with} \quad S = \left(\frac{dF}{dh}\right)_{h=h_{max}} \tag{8}$$

where H is defined as the indentation hardness, M is the indentation modulus, F_{max} is the maximum applied force on the indenter, h_{max} is the maximum penetration depth, A_c is the projected contact area on the sample, and S is the stiffness of the unloading curve at h_{max} (see Figure 8).

Indentation hardness is related to the elastic-plastic response of the material; however, it cannot be directly related to the conventional plastic parameters such as the angle of friction and cohesion. Therefore, this mechanical property is mainly derived for comparison of different material responses. The indentation modulus, on the other hand, can be analytically related to the elastic constants of the material. For isotropic (equation 9) and transversely isotropic (equations 10 and 11) materials, it can be written as (Delafargue and Ulm 2004):

$$M = \frac{E}{1-\nu^2} = \frac{C_{11}^2 - C_{12}^2}{C_{11}} \tag{9}$$

$$M_3 = 2\sqrt{\frac{C_{11}C_{33} - C_{13}^2}{C_{11}}\left(\frac{1}{C_{44}} + \frac{2}{\sqrt{C_{11}C_{33}} + C_{13}}\right)^{-1}} \tag{10}$$

$$M_2 \approx \sqrt{\frac{C_{11}^2 - C_{12}^2}{C_{11}}\sqrt{\frac{C_{11}}{C_{33}}}M_3} \tag{11}$$

where M_3 is the indentation modulus when the indenter is perpendicular to bedding direction whereas M_1 is the indentation modulus when the indenter is parallel to bedding direction.

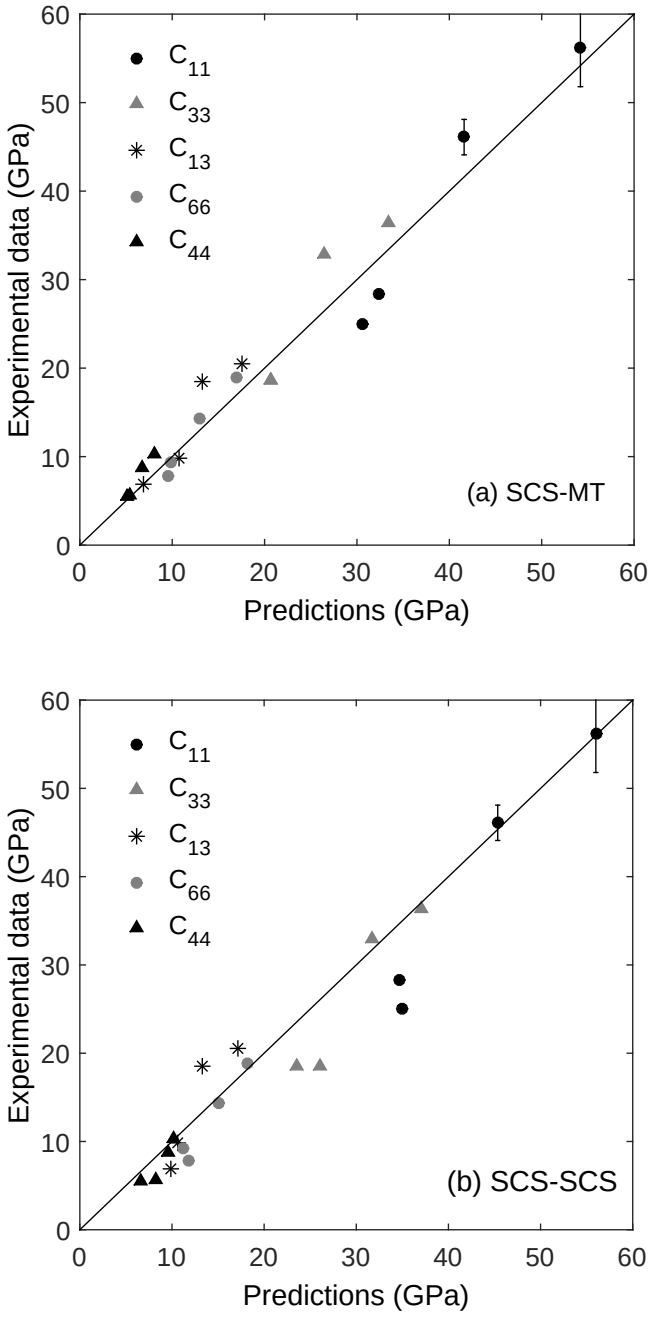

Figure 7: Summary of the experimental and predicted results for the UPV data sets shale samples using (a) SCS-SCS and (b) SCS-MT.

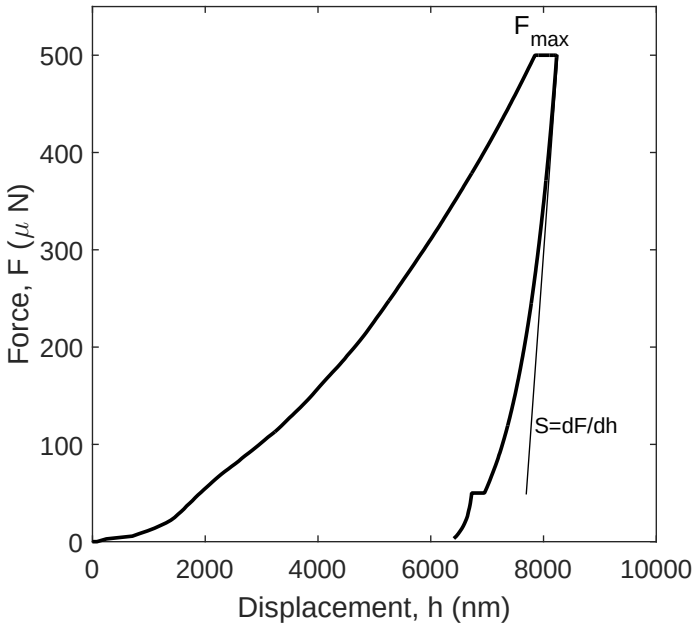

Figure 8: Loading-unloading curve versus displacement for a single indentation test on a shale thin section.

5.3.2 Petrological characterisation and sample mechanical properties

The Toarcian shales of the Paris Basin are the lateral equivalent of the Northern European Posidonia Shale, consisting of a sequence of marine shales deposited in the Tethys Ocean during the Early Jurassic. The Toarcian shales are rich in organic material and have shale oil potential (Jarvie 2012). Our samples come from the Couy-1 well which was drilled in 1986-1987. Toarcian shales are located between 210 m and 355 m (Pradier and Gauthier 1987).

Core samples of the Toarcian shales were selected from different depths based on the quality of the samples. QEMSCAN analysis was used to determine the mineralogy of the selected samples. QEMSCAN is an automated mineralogy method that combines electron microscopy with energy dispersive spectroscopy for quantitative mineralogical analysis of rock sample. Based on the mineralogical data, four samples were selected for indentation measurements to determine the mechanical properties. Figure 9 shows digital mineralogical image generated by QEMSCAN analysis. Table 8 provides information about the total organic carbon, T_{max} index and mineralogical descriptions for the samples used in indentation tests. The following empirical relationship has been used to convert the TOC in weight percent to kerogen in volume percent (Vernik and Nur 1992; Carcione 2000):

$$K_r = \frac{\mathrm{TOC}\rho_\mathrm{b}}{0.75\rho_k} \tag{12}$$

where ρ_b is the bulk density of the sample, ρ_k is the kerogen density and K_r is the volumetric kerogen content. The values of T_{max} are less than 435 indicating that the shale samples are immature; therefore, a value of 1.25 g/cm^3 was selected for the kerogen density (Okiongbo, Aplin and Larter 2005).

For each shale sample two surfaces, one parallel and one perpendicular to bedding, were prepared and polished in order to provide relatively smooth area as for the PeakForce QNM® tests. Tests were performed using the Berkovich indenter along with a force-controlled condition with a maximum value of 400 mN set for all experiments. This maximum possible load was applied in order to create the maximum possible contact area and to obtain the best surface response of the whole shale composite. This force value generated indentation depths from 3.5 μm to 6.5 μm, depending on the sample stiffness.

Due to the complex nature of shale, even at the scale of a few microns, a large number of indents must be conducted in order to obtain a robust statistical description of the mechanical response. Here, an average, around 80 indentations were conducted on each surface to characterise its mechanical response. It should be noted that the indentation data usually contains some out-of-range values which might be caused by the indenter mainly touching a large stiff grain or a large pore space, generating very high or very low penetration depths, respectively. A judgment is hence required to filter the out-of-range data and to eliminate their effects on the calculation of mean and standard deviation of shale material properties (Table 9).

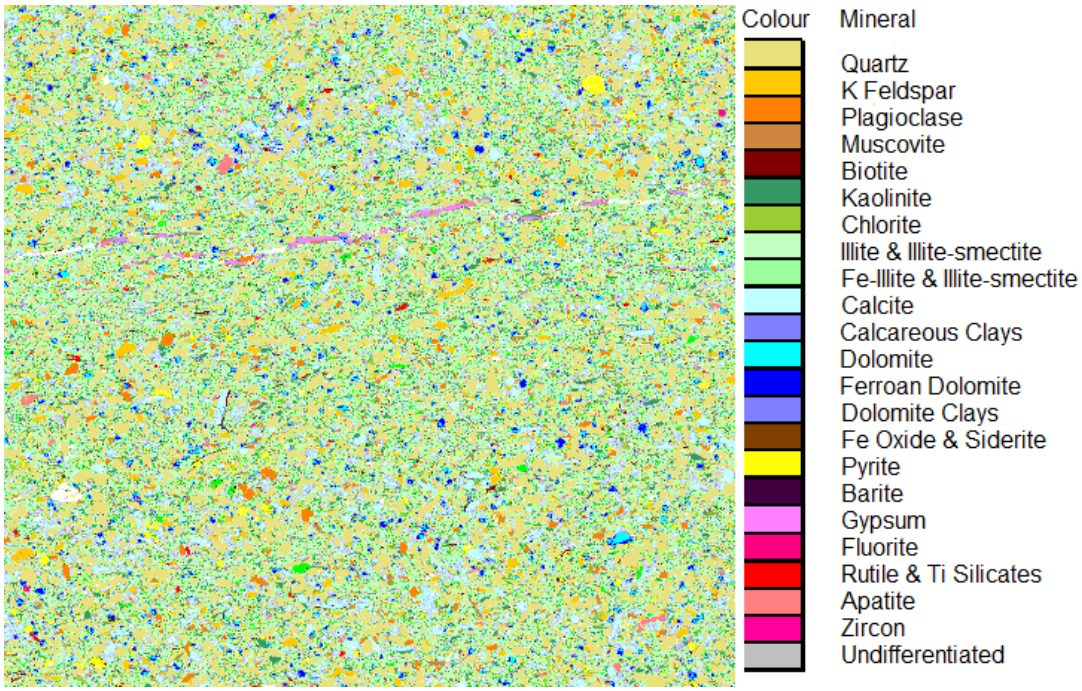

Figure 9: QEMSCAN image based on combination of SEM and EDS digital images.

Table 8: Rock-Eval and volumetric mineralogical data for the indentation test shale samples.

Sample No.	2	6	8	10
Quartz	29.3	6.5	9.3	25.6
Calcite	0.8	7.4	9.6	5.8
Pyrite	0.3	1.1	6.1	2.7
Feldspar	3.6	0.2	0.6	2.6
Dolomite	1. 5	2.7	1.6	1.1
Total silt inclusions	35.4	17.9	27.1	37.9
Kerogen	3.2	5.6	19.5	3.2
Porous Clay	61.3	87.68	53.4	58.9
T_{max}	432	430	419	432
TOC (Weight %)	1.1	2.0	7.5	1.1
Bulk density (g/cm^3)	2.65	2.67	2.45	2.66
Depth (m)	224.9	340	347.5	202.5

In order to better understand the source of anisotropy in these samples the anisotropy ratio (M_1/M_3) is plotted versus kerogen volume fraction in Figure 10. It can be observed that an increase in kerogen does not necessarily translate into increased anisotropy but reduces both indentation moduli significantly. This result contrasts with the correlation between anisotropy and the kerogen volume fraction suggested by Vernik and Nur (1992). However, observations from experiments reported in Vernik and Landis (1996) and Kumar (2012) show that the correlation between kerogen volume fraction and Thomsen's anisotropic parameter ε is relatively weak. In fact, the reported data are scattered, particularly on immature samples (Vernik and Nur 1992), which further reveals the difficulties involved in the determination of the main parameters affecting shale anisotropy.

Table 9: Indentation moduli (GPa).

Sample Sample No.	M_1 (GPa)		M_3 (GPa)		Anisotropy ratio M_1/M_3
	Mean	SD	Mean	SD	
2	30.3	7.7	17.2	7.3	1.76
6	27.4	2.7	17	2.1	1.61
8	20.6	2.8	12.6	2.5	1.63
10	28.5	7.6	-	-	-

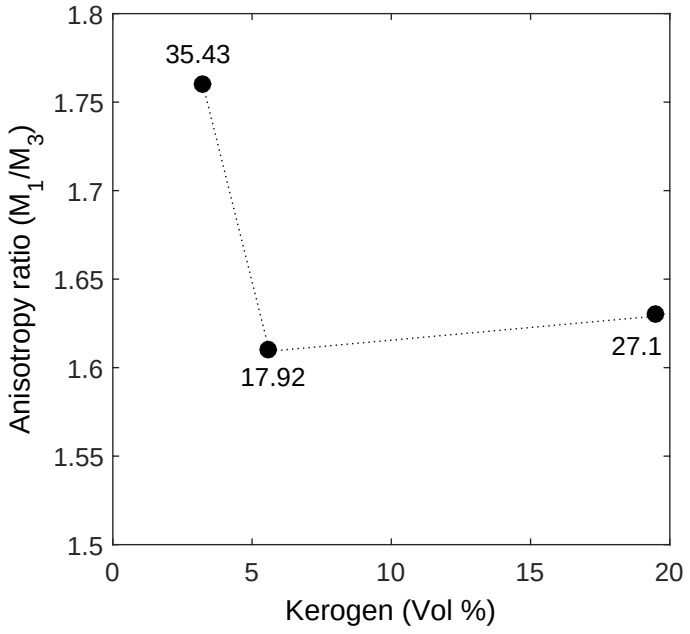

Figure 10: Anisotropy versus kerogen volume fraction (data label is the volume fraction of silt inclusions).

5.3.3 Homogenisation of organic-rich shales

In order to calculate the indentation moduli from the homogenisation technique, porosity and organic matter content should also be taken into account, in addition to the mineralogical data provided in Table 8. Here, an estimation of the porosity is required as this parameter was not measured. In addition, identifying the material properties of organic matter and its role on the overall mechanical behaviour of the shale composite is also important.

Due to the fact that all the samples have been retrieved from similar depths (see Table 8), it is assumed that the clay packing density, η , is the same in all samples. The clay packing density relates to the compaction state of clay particles and can be defined as: $\eta = 1 - \phi_{clay}$. This value can be back-calculated from one data set by equalising the experimental value to the predicted one. The obtained value is then used as the 'reference parameter' for the rest of the experimental data. In addition, as the sample had been exposed to room-temperature for a long time before the test, the shale will be considered as dry, with no fluid within the pore spaces.

An assumption in the homogenisation formulation is that the matrix is considered as a continuous phase and the inclusions are isolated and fully surrounded by the matrix phase. SEM observations (see Figure 3) suggest that the organic matter is a semi-continuous phase mixed with the porous clay. We therefore assume that the organic matter can be considered to be part of the shale matrix so that its contribution is taken into account, along with that of the porosity, in the first level of homogenisation. Previous approaches include considering organic matter as the background phase in shale (Vernik and Landis 1996, Bayuk et al. 2008; Sayers 2013b), combining kerogen and solid clay as the elementary building block of the shale matrix, or adding kerogen as inclusions (Guo et al. 2014).

Based on the observation that kerogen in the tested samples does not increase the anisotropy ratio, it is assumed here that kerogen is mixed with a porous clay having the same packing density in all the samples. The combination of these phases through the use of SCS enables us to reproduce a system of semi-continuous random pore and kerogen networks with no preferential orientation. This approach is consistent with the experimental observation (Figure 10) in which anisotropy is slightly reduced by an increase in kerogen. The mechanical properties of kerogen are an important and controversial factor in the prediction of the overall mechanical response for organic-rich shale. However, as discussed in Section 3, there is a discrepancy between the reported elastic properties of kerogen in the literature. In Section 4, the nanoscale direct mechanical measurements were conducted on an immature shale sample which provided a mean value of 6 GPa for kerogen assuming that the Poisson's ratio is 0.3. As the current samples are also immature, this value will be adopted for the micromechanical modelling.

Based on the predicted results in Section 5.2, the SCS homogenisation strategy was also considered at the second level. The clay packing density was calibrated to be approximately 0.75 based on the indentation modulus parallel to the bedding direction (M_1) for sample No. 2. The same packing density was adopted for the remaining samples. Figure 11 summarizes the experimental data versus the predicted values for indentation moduli. Table 10 also provides these values along with their relative errors.

Considering the standard deviations in the indentation data, which create a range for the indentation moduli, it can be seen that almost all the predicted moduli are within these ranges. The model shows very good predictions of the effect of changing the kerogen and inclusion volume fractions purely based on mineralogical composition. However, in two cases of samples No. 2 and No. 8, the experimental data show a higher anisotropy ratio (M_1/M_3) than the predictions. This could be attributed to the simplifications which assume spherical silt inclusions and pores/kerogen distributions with no preferential orientation. In addition, the presence of microfractures could significantly contribute to the higher anisotropy of the experimental results (Sayers 2013a). Kanitpanyacharoen et al. (2010) and Vasin et al. (2013) have determined some of the textural effects by quantifying orientation distributions and shapes of the minerals in different shale samples. An advanced micro-mechanical modelling approach used in these studies, accounting for experimental data, did not result in satisfactory predictions in terms of P-wave velocities and anisotropy. They concluded that the differences in model and experimental results could be attributed to the anisotropy and weaknesses induced by oriented pore structures, microfractures and kerogen. Although these effects can easily be introduced into the model by considering an elliptical shape for silt inclusions, pores and kerogen, it is very difficult to quantify the effects by direct experimental measurements. Bayuk et al. (2008) found that when these micro-structural features are unknown, considering different combinations of them in the modelling can produce similar anisotropy. This is one of the drawbacks of micro-mechanical modelling and also one of the reasons why a range of modelling strategies has been adopted for shale. In fact, it is not reasonable to add more complexity to the modelling while the input parameters are not quantitatively known. The idea of using a set of TI parameters for solid clay as the main source of anisotropy is a simplified yet reasonably accurate approximation for a more complex shale structure. A possible solution could be to combine micro-mechanical modelling with fast and efficient indentation testing on shale cuttings, which cannot solely characterise full TI elastic constants of shales, in order to identify some of the potential sources of anisotropy and also calibrate the micro-structural features.

Table 10: Predicted results (Pred.) versus experimental measurements (Exp.).

Sample No.	Clay packing density	Exp. M_1 (GPa)	Exp. M_3 (GPa)	Exp. M_1/M_3 -	Pred. M_1 (GPa)	Pred. M_3 (GPa)	Pred. (M_1/M_3) -	Error M_1 (%)	Error M_3 (%)
2	0.75	30.3	17.2	1.76	30.3	21.6	1.4	0.0	25
6	0.75	27.4	17	1.61	26.5	17.1	1.55	3.5	0.5
8	0.75	20.6	12.6	1.63	18.8	13.9	1.33	9	11.9
10	0.75	28.5	-	-	30.6	22.7	-	7.3	-

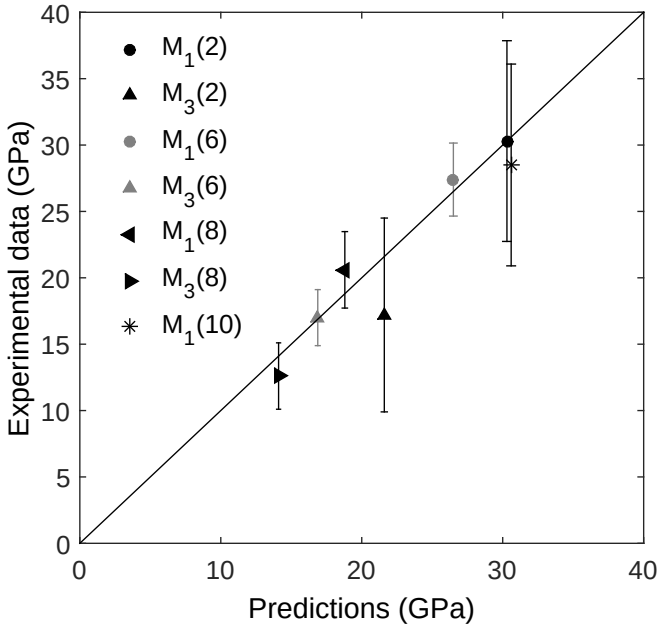

Figure 11: The experimental and predicted values for indentation moduli (vertical bars represent the standard deviations for the experimental data).

6 Conclusions

We have studied the capabilities of a range of multi-scale homogenisation techniques to model and predict the elastic response of shales. The shales were assumed to be a composite formed by a matrix containing solid clay, kerogen and pores. Solid mineral grains/inclusions were randomly distributed within the matrix. Consequently, two levels of homogenisation were required involving the SCS method at the first level to upscale the shale matrix and, at the second level, the capabilities of both MT and SCS in homogenising the matrix-inclusion morphology.

Resulting Young's modulus maps using the AFM-based PeakForce QNM® mechanical characterisation mode on two sections of immature, organic-rich shale, showed an isotropic response for quartz grains. The porous clay, in contrast, showed highly anisotropic behaviour with almost the same anisotropy ratio as measured at the macroscale. Organic matter is seen to be a semi-continuous phase within the porous clay matrix, with a measured Young's modulus of 6 GPa.

Results from the homogenization method were evaluated against the limited geomechanical datasets available in the literature. Considering the multiscale complexity of shales and also the high standard deviations usually obtained in mechanical experiments on shale samples, the values estimated by the homogenisation method, which are based solely on mineralogical descriptions, provide valuable predictions of the mechanical response. Additionally, comparing SCS and MT for the second level of homogenisation, it was concluded that SCS produced a slightly better prediction of elastic response with a very good estimate of anisotropy.

Finally, to generate more data for organic-rich shales easily and inexpensively, advanced indentation tests were implemented. Based on the observations in the nanoscale mechanical maps, organic matter was taken into account in the first level of homogenization with the elastic modulus being measured by nano-mechanical mapping. A comparison between the predicted indentation moduli and the experimental values confirms the capability of the multi-scale homogenization method to predict the effect of kerogen on the elastic response of shales, provided that this phase is suitably accounted for. However, micro-structural features such as grain shape or pore aspect ratio, which cannot be measured directly, need to be calibrated in order to further adjust the predicted anisotropy. This calibration can be performed with indentation data sets which can be obtained from shale cuttings. Generally, it can be concluded that the homogenization technique can be effectively used as an auxiliary approach to conventional rock mechanics tests to estimate the elastic response of shale rocks using petrological and mechanical properties of shale cuttings.

Acknowledgements

The authors would like to acknowledge the collaboration of the BRGM (the French geological survey) and SGS Horizon B.V. by providing shale samples characterisation and the experimental indentation data. The first author

greatly acknowledges discussions with Mr. Leon Bowen on sample preparation, SEM and EDS analyses. We also thank Dr. Richard Thompson for providing access to the AFM facilities at Durham University. The anonymous reviewers are thanked for their valuable comments which helped to improve the manuscript.

Rerefences

Amirmajdi O.M., Ashyer-Soltani R., Clode M.P., Mannan S.H., Wang Y., Cabruja E. and Pellegrini G. 2009. Cross-section preparation for solder joints and MEMS device using argon ion beam milling. *IEEE Transactions on electronics packaging manufacturing* **32**(4), 265-271.

Antonangeli D., Krish M., Fiquet G., Badro J., Farber D.L., Bossak A. and Merkel S. 2005. Aggregate and single-crystalline elasticity of hcp cobalt at high pressure. *Physical Review B* **72**, 134303.

Aplin A.C. and Macquaker J.H.S. 2011. Mudstone diversity: origin and implications for source, seal and reservoir properties in petroleum systems. *The American Association of Petroleum Geologists (AAPG) Bulletin* **95**(12), 2031-2059.

Bass J.D. 1995. Elasticity of minerals, glasses, and melts. In: *Minerals Physics & Crystallography: A handbook of physical constants* (ed. T.J. Ahrens), pp. 45-63. *AGU Reference Shelf*. ISBN 9780875908526.

Bayuk I.O., Ammerman M. and Chesnokov E.M. 2008. Upscaling of elastic properties of anisotropic sedimentary rocks. *Geophysical Journal International* **172**, 842-860.

Bobko C. and Ulm F.J. 2008. The nano-mechanical morphology of shale. *Mechanics of Materials* **40**, 318-337.

Bruker's Application Note #141. Toward quantitative nanomechanical measurements on live cells with PeakForce QNM. https://www.bruker.com/products.

Bruker's Application Note #128. Quantitative mechanical property mapping at the nanoscale with PeakForce QNM. https://www.bruker.com/products.

Carcione J.M. 2000. A model for seismic velocity and attenuation in petroleum source rocks. *Geophysics* **65**(4), 1080-1092

Chalmers G.R., Bustin R.M. and Power I.M. 2012. Characterization of gas shale pore systems by porosimetry, pycnometry, surface area, and field emission scanning electron microscopy/transmission electron microscopy image analyses: Examples from the Barnett, Woodford, Haynesville, Marcellus and Doig units. *The American Association of Petroleum Geologists (AAPG)* **96**(6), 1099-1119.

Delafargue A. and Ulm F.J. 2004. Explicit approximations of the indentation modulus of elastically orthotropic solids for conical indenters. *International Journal of Solids and Structures* **41**, 7351-7360.

Domnesteanu P., McCann C. and Sothcott J. 2002. Velocity anisotropy and attenuation of shale in under- and over pressured conditions. *Geophysical Prospecting* **50**, 487-503.

Draege A., Jakobsen M. and Johansen T.A. 2006. Rock physics modelling of shale diagenesis. *Petroleum Geoscience* **12**, 49-57.

Eliyahua M., Emmanuel S., Day-Stirrat R.J. and Macaulay C.I. 2015. Mechanical properties of organic matter in shales mapped at the nanometer scale. *Marine and Petroleum Geology* **59**, 294-304.

Fritsch A. and Hellmich C. 2007. Universal microstructural patterns in cortical and trabecular, extracellular and extravascular bone materials: Micromechanics-based prediction of anisotropic elasticity. *Journal of Theoretical Biology* **244**, 597-620.

Goodarzi M., Rouainia M. and Aplin A.C. 2016. Numerical evaluation of mean-field homogenisation methods for predicting shale elastic response. *Computational Geosciences* **20**, 1109-1122.

Guo Z.Q., Li X.Y. and Liu C. 2014. Anisotropy parameters estimate and rock physics analysis for the Barnett Shale. *Journal of Geophysics and Engineering* **11**, 065006.

Heyliger P., Ledbetter H. and Kim S. 2003. Elastic constants of natural quartz. *The Journal of the Acoustical Society of America* **114**, 644-650.

Hill R. 1965. A self-consistent mechanics of composite materials. *Journal of Mechanics and Physics of Solids* **13**,

213-222.

Hornby B.E., Schwartz L. and Hudson J. 1994. Anisotropic effective medium modelling of the elastic properties of shales. *Geophysics* **59**, 1570-83.

Hornby B.E. 1998. Experimental laboratory determination of the dynamic elastic properties of wet, drained shales. *Journal of Geophysical Research* **103**(B12), 29945-29964.

Jakobsen M. and Johansen T.A. 2000. Anisotropic approximations for mudrocks: A seismic laboratory study. *Geophysics* **65**(6), 1711-1725.

Jakobsen M., Hudson J.A. and Johansen T.A. 2003. T-matrix approach to shale acoustics. *Geophysical Journal International* **154**, 533-558

Jarvie D.M. 2012. Shale resource systems for oil and gas: Part 2 Shale-oil resource systems. In: *Shale reservoirs Giant resources for the 21st century* (ed. J.A. Breyer), pp. 89-119. AAPG Memoir Volume **97**. ISBN 978-1-62981-011-9.

Jones L.E.A. and Wang H.F. 1981. Ultrasonic velocities in Cretaceous shales from the Williston basin. *Geophysics* **46**(3), 288-297.

Kanitpanyacharoen W., Wenk H.R., Kets F., Lehr C. and Wirth R. 2011. Texture and anisotropy analysis of Qusaiba shales. *Geophysical Prospecting* **59**, 536-556.

Klusemann B., Bohm H.J. and Svendsen B. 2012. Homogenisation methods for multi-phase elastic composites with non-elliptical reinforcements: Comparisons and benchmarks. *European Journal of Mechanics - A/Solids* **34**, 21-37.
Kumar V., Sondergeld C.H. and Rai C.H. 2012. Nano to macro mechanical characterization of shale. SPE Annual Technical Conference and Exhibition, San Antonio, Texas, USA. SPE 159804.

Kumar V. 2012. Geomechanical Characterization of Shale Using Nano-indentation. MSc dissertation, University of Oklahoma.

Laws N. 1977. The determination of stress and strain concentrations at an ellipsoidal inclusion in an anisotropic material. *Journal of Elasticity* **7**(1), 91-97.

Mavko G., Mukerji T. and Dvorkin J. 2009. The Rock Physics Handbook. Cambridge University Press. ISBN 9780521861366.

Mori T. and Tanaka K. 1973. Average stress in matrix and average elastic energy of materials with misfitting inclusions. *Acta Metallurgica* **21**, 571-574.

Mortazavi B., Baniassadi M,. Bardon J. and Ahzi S. 2013. Modelling of two-phase random composite materials by finite element, Mori-Tanaka and strong contrast methods. *Composites: Part B* **45**, 1117-1125.

Okiongbo K.S., Aplin A.C. and Larter S.R. 2005. Changes in Type II Kerogen Density as a Function of Maturity: Evidence from the Kimmeridge Clay Formation. *Energy & Fuels* **19**, 2495-2499.

Ortega J.A., Ulm F.J. and Abousleiman Y. 2007. The effect of the nanogranular nature of shale on their poroelastic behaviour. *Acta Geotechnica* **2**, 155-182.

Ortega J.A., Ulm F.J. and Abousleiman Y. 2010. The effect of particle shape and grain-scale properties of shale: A micromechanics approach. *International Journal of Numerical and Analytical Method in Geomechanics* **34**, 1124-1156.

Peng S., Yang J., Xiao X., Loucks B., Ruppel S. and Zhang T. 2015. An integrated method for upscaling pore-network characterization and permeability estimation: example from the Mississippian Barnett shale. *Transport in Porous Media* **109**, 359-376.

Pradier B. and Gauthier B. 1987. Etude préliminaire de la matière organique sédimentaire. In: *Géologie profonde de la France, forage scientifique de Sancerre-Couy* (ed. C. Lorenz), pp. 103-108. Documents n^{o}135 du Bureau de Recherches Géologiques et Minières (BRGM). in French

Qin X., Han D. and Zhao L. 2014. Rock physics modeling of organic-rich shales with different maturity levels. *SEG*

Technical Program Expanded Abstracts, 2952-2957.

Sayers C.M. 1994. The elastic anisotropy of shales. *Journal of Geophysical Research* **99**(B1), 767-774.

Sayers C.M. 2013a. The effect of anisotropy on the Young's moduli and Poisson's ratios of shales. *Geophysical Prospecting* **61**, 416-426.

Sayers C.M. 2013b. The effect of kerogen on the elastic anisotropy of organic-rich shales. *Geophysics* **78**, (2), D65-D74.

Sierra R., Tran M.H., Abousleiman Y.N. and Slatt R.M. 2010. Woodford Shale Mechanical Properties and the Impacts of Lithofacies. The 44th US Rock Mechanics Symposium and 5th US-Canada Rock Mechanics Symposium. Salt Lake City ARMA-10-461

Trtik P., Kaufmann J. and Volz U. 2012. On the use of peak-force tapping atomic force microscopy for quantification of the local elastic modulus in hardened cement paste. *Cement and Concrete Research* **42**, 215-221.

Ulm F.J. and Abousleiman Y. 2006. The nanogranular nature of shale. *Acta Geotechnica* **1**, 77-88.

Vasin R.N., Wenk H.R., Kanitpanyacharoen W., Matthies S. and Wirth R. 2013. Elastic anisotropy modeling of Kimmeridge shale. *Journal of Geophysical Research: Solid Earth* **118**, 3931-3956.

Vernik L. and Nur A. 1992. Ultrasonic velocity and anisotropy of hydrocarbon source rocks. *Geophysics* **57**, 727-735.

Vernik L. and Landis C. 1996. Elastic anisotropy of source rocks: Implication for HC generation and primary migration. *AAPG Bulletin* **80**, 531-544.

Vernik L. and Milovac J. 2011. Rock physics of organic shales. *The Leading Edge* **30**, 318-323.

Wang Z., Wang H. and Cates M.E. 2001. Effective elastic properties of solid clays. *Geophysics* **66**(2), 428-440.

Whitaker M.L., Liu W., Wang L. and Li B. 2010. Acoustic velocities and elastic properties of Pyrite (FeS2) to 9.6 GPa. *Journal of Earth Science* **21**, 792-800.

Wu X., Chapman M., Li X.Y. and Dai H. 2012. Anisotropic elastic modelling for organic shales. 74th EAGE Conference and Exhibition SPE EUROPE, Copenhagen, Denmark, P314

Yan F. and Han D. 2013. Measurement of elastic properties of kerogen. 83rd SEG Annual Meeting, Houston, USA, Expanded Abstracts, 2778-2782

Zargari S., Prasad M., Mba K.C. and Mattson E.D. 2013. Organic maturity, elastic properties, and textural characteristics of self-resourcing reservoirs. *Geophysics* **78**(4), D223-D235.

Zeszotarski J.C., Chromik R.R., Vinci R.P., Messmer M.C., Michels R. and Larsen J.W. 2004. Imaging and mechanical property measurements of kerogen via nanoindentation. *Geochimica et Cosmochimica Acta* **68**, 4113-4119.

Zhu Y., Xu S., Payne M., Martinez A., Liu E., Harris C. and Bandyopadhyay K. 2012. Improved rock-physics model for shale gas reservoirs. 82nd SEG Meeting, Denver, USA, Expanded Abstracts 2952-2957.

Zu Y., Xu S., Liu E., Payne M.A. and Terrell M.J. 2013. Predicting anisotropic source rock properties from well data: U.S. Patent 2013/0013209 A1.